AIAA SciTech Forum
4-8 January 2016, San Diego, California, USA
54th AIAA Aerospace Sciences Meeting

10.2514/6.2016-0244

Laser Ablation of Dielectrics for Development of High Temperature Sapphire Based Pressure Transducers

Peter Woerner* and William Oates†
Florida State University, Tallahassee, FL, 32310, USA
Daniel Blood‡
Valparaiso University, Valparaiso, IN, 46383, USA
Mark Sheplak§and David Mills¶
University of Florida, Gainesville, FL, 32611, USA

High temperature pressure sensing is desirable for a broad range of applications such as structural health monitoring of space vehicles and control of combustion processes; however, limited materials for sensor design can sustain temperatures above 1000°C while under time-varying pressure. A sapphire based optical pressure transducer has been proposed for measuring pressure at temperatures approaching 1600°C. Manufacturing such sensors has focused on picosecond laser machining. Current research has produced models which can predict ablation depth for longer (ns) pulses and shorter (fs) pulses but there is an underwhelming amount of research focusing on predicting and understanding the mechanics of picosecond pulses. We put forth a model for laser ablation using Maxwell's equations and a sharp interface limit of the Allen-Cahn equation and compare different constitutive laws which couple the two equations together. The proposed modeling results are compared to laser machining experimental data on sapphire to illustrate key material parameter uncertainty and sensitivity to the laser machining process. Bayesian uncertainty quantification is used to help validate the approximations within the constitutive equations.

I. Introduction

High powered laser-sapphire interactions have long been of interest to those studying fundamental physics. This research has found numerous engineering applications including microfluidics, microsensors, optical windows, abrasion resistant mechanical contacts, buffer materials and high power laser construction.[1–3] Therefore, numerous computational and experimental studies have been performed regarding milli-, micro-, nano-, pico- and femtosecond laser ablation. The first step of light-matter interaction is non-thermal absorption (electron excitation) through either multiphoton ionization, defect allowed single-photon ionization or inverse Bremsstrahlung.[1,4] Only multiphoton ionization is allowed in pristine equilibrium sapphire on the basis of sapphire's large bandgap energy of $\approx$ 8.8eV.[5] Absorption is followed by complex material processes. In general this secondary process is classified as either photothermal (pyrolytic), photochemical (photolytic) or photophysical (both thermal and chemical). This classification is difficult because it can depend on many different parameters including laser pulse duration, fluence, material properties and material defects.[6] Conventionally, pulse length is considered the leading determinant of classification.[7] However, experimental

*pcw13@my.fsu.edu
†woates@fsu.edu
‡daniel.blood@valpo.edu
§sheplak@ufl.edu
¶dm82@ufl.edu

measurements have shown that sapphire is unconventional.[8–12] Millisecond pulses have been quantified to produce thermal melting.[5] Nanosecond pulses ablate via electron sputtering,[8] a photochemical process. This is concluded from temperature measurements of the ablation plume.[9,10] Faster pico- and femtosecond pulsed laser-sapphire interactions have proven to be more complex.

The complexity of pico- and femtosecond pulsed laser interaction is strongly dependent on material defects. Defects play a large role in laser induced damage of dielectrics.[13] Nowhere can this be seen more clearly than in sapphire's two ablation phases: the gentle phase and the strong phase.[8] Experimental results have suggested that the transition from the gentle to strong phase is due to the number of defects and inclusions in the material.[8] The gentle phase is characterized by a lower rate of removal and a polishing surface effect while the strong phase has a significantly larger rate of removal and tends to have a rough surface finish.[11] Although separate gentle and strong phases do not generally exist in other dielectrics,[12] these materials still see huge variability in ablation depth and threshold due to defects.[13] The gentle phase is considered to be a photochemical effect: either Coulomb explosion or particle vaporization while the strong phase is considered to be a photothermal effect, specifically phase explosion.[11,14] This separation into gentle and strong phases works well when the laser pulse is $\tau_{pulse} \lesssim 4$ps; however the physical characteristics begin to blend together when $\tau_{pulse} \gtrsim 4$ps.[11] This leaves classification of picosecond lasers an open question.

In this paper, we put forth a model for laser ablation based on Maxwell's equations and a phase field formulation in the sharp interface limit. The equations are then coupled through constitutive laws which contain uncertainties associated with the laser ablation process. Section II presents the underlying equations used to represent laser ablation. Section III presents numerical approximations, implementation, uncertainty analysis and results. Section IV presents the conclusions.

II. Governing Equations

II.A. Material Kinetics

The kinetic relations governing light-matter interactions of sapphire start with a phase field or diffuse interface model that tracks the interface between air and the solid material.[15] This is described by the Allen-Cahn equation

$$\beta \frac{\partial \rho}{\partial t} + \frac{\partial \Sigma}{\partial \rho} = \left(\frac{\partial \Sigma}{\partial \rho_{,i}} \right)_i + \gamma \tag{II.1}$$

where ρ is a scalar parameter governing the underlying electronic structure of the material, Σ is the stored energy per undeformed volume, and γ is an external potential that forces the material from a low energy crystal state and to a higher energy excited state. A more general framework that defined electronic structure vector order parameters is given by Nelson.[16] Lastly, gradients on the order parameter $\left(\rho_{,i} = \frac{\partial \rho}{\partial x_i}\right)$ are included to accommodate surface and interface energy between sapphire and air.

The stored energy is defined as a function of the order parameter and its gradient. This approximates the material behavior in terms of its electronic structure as an effective density. Since no mechanical loads are directly applied during laser machining we neglect the internal stress effects on the electronic structure evolution. The stored energy then takes the form

$$\Sigma = \frac{a}{4}\rho^2(\rho - 1)^2 + \frac{a_0}{2}\rho_{,i}\rho_{,i} \tag{II.2}$$

where a is the Landau parameter governing the strength of the atomic bonds in the solid and a_0 is a gradient parameter governing gradient energy.

In the limiting case, we consider a sharp boundary by setting a_0 to 0. This reduces the partial differential equation (PDE) in (II.1) to the following ODE which needs to be solved at every point

$$\beta \frac{\partial \rho}{\partial t} = -a(\rho - 1)(\rho - \frac{1}{2})(\rho) + \gamma \tag{II.3}$$

.

The external potential, γ in this model, is due to the light source. Its effect on electronic structure evolution requires solving the electromagnetic field associated with light. These fields are described in the following section which is followed by methods to couple the fields to laser ablation via γ.

II.B. Electromagnetics

The phase field equation equation is coupled with Maxwell's time dependent field equations using the form

$$\begin{aligned} \boldsymbol{\nabla}\cdot\boldsymbol{D} &= \rho_f \quad \boldsymbol{\nabla}\times\boldsymbol{E} = -\frac{\partial \boldsymbol{B}}{\partial t} \\ \boldsymbol{\nabla}\cdot\boldsymbol{B} &= 0 \quad \boldsymbol{\nabla}\times\boldsymbol{H} = \boldsymbol{J}_f + \frac{\partial \boldsymbol{D}}{\partial t} \end{aligned} \tag{II.4}$$

where $\boldsymbol{E}$ is the electric field, $\boldsymbol{B}$ is the magnetic induction field, ρ_f is the free charge, $\boldsymbol{D}$ is the electric displacement, $\boldsymbol{H}$ is the magnetic field, and $\boldsymbol{J}_f$ is the free current. Assuming a homogeneous isotropic linear media, the constitutive relations include

$$\boldsymbol{D} = \epsilon\boldsymbol{E}, \quad \boldsymbol{H} = \tfrac{1}{\mu}\boldsymbol{B}, \quad \boldsymbol{J} = \sigma\boldsymbol{E} \tag{II.5}$$

where ϵ is the dielectric permittivity, μ is the material permeability and σ is the electrical conductivity. Substitution of (II.5) into (II.4) leads to

$$\begin{aligned} \boldsymbol{\nabla}^2\boldsymbol{E} &= \mu\epsilon\frac{\partial^2 \boldsymbol{E}}{\partial t^2} + \mu\sigma\frac{\partial \boldsymbol{E}}{\partial t} \\ \boldsymbol{\nabla}^2\boldsymbol{B} &= \mu\epsilon\frac{\partial^2 \boldsymbol{B}}{\partial t^2} + \mu\sigma\frac{\partial \boldsymbol{B}}{\partial t} \end{aligned} \tag{II.6}$$

An analytic solution for plane waves traveling in the x direction of (II.6) is

$$\boldsymbol{E} = \boldsymbol{E}_0 \mathrm{e}^{-\kappa x}\mathrm{e}^{\mathrm{i}(\bar{k}x-\omega t)} \tag{II.7}$$

where κ is the attenuation factor which is related to the skin depth by $d \equiv \frac{1}{\kappa}$ where $d \approx \sqrt{\frac{2}{\omega\sigma\mu_0}}$, $\bar{k} \approx \sqrt{\frac{\omega\sigma\mu_0}{2}}$ is the wave number.[17] The nonlinear Beer type approximation is given by

$$\frac{\partial\langle|E|\rangle}{\partial x} = -\kappa\langle|E|\rangle \tag{II.8}$$

where $\kappa = \kappa(\rho)$ A Beer Law relation derivation can be found in any number of textbooks on electromagnetic wave propagation, see for example.[17] The nonlinear form can be justified by the similar forms found in the literature.[6,18,19] Alternatively, if we treat our space as a series of different materials of length Δx but with different absorption coefficients we have, $\lim_{\Delta x\to 0}\frac{\partial<E>}{\partial x} = -\kappa(x)E$.

II.C. Coupling

While both the electromagnetic and material kinetics are well established in the literature, there exists uncertainty in the nature of their coupling. The equations are coupled in two ways. First through the driving force γ and second through the attenuation factor, κ.

The driving force is given by the standard equation for the electromagnetic force

$$\gamma = |qE| \tag{II.9}$$

where q is the charge density.[16] This represents a formulation based on the forces applied to the electronic structure.

The total charge density is given by a Taylor expansion on higher order poles within the material as

$$q = q_0 - \nabla\cdot\boldsymbol{P} + \nabla\nabla : \underline{\underline{\boldsymbol{Q}}} + ... \tag{II.10}$$

where $\boldsymbol{P}$ is the polarization and $\underline{\underline{\boldsymbol{Q}}}$ is the next higher order quadrupole moment. The free charge is denoted by q_0. During laser ablation, insulators such as sapphire transition locally to an effective conducting solid as the material reaches a sufficiently high excited state. This means the terms within (II.10) evolve during laser ablation.

The total charge density is therefore written as

$$q(\rho, E) = q_0(\rho, E) + q_b(\rho, E) \tag{II.11}$$

where the bound charge density is $q_b(\rho, E) = -\nabla \cdot \boldsymbol{P} + \nabla\nabla : \underline{\underline{\boldsymbol{Q}}}$ and $q_0(\rho, E)$ is the free charge density.

Expanding q in a Taylor series about $|E| = 0$ gives

$$q = q_1 + q_2|E| + \frac{q_3}{2!}|E|^2 + ... \tag{II.12}$$

Truncating to first oreder leaves

$$q = q_1 + q_2|E| \tag{II.13}$$

or the scalar form

$$q = q_1 \tag{II.14}$$

It is uncertain, *a priori* when one should truncate the series terms.

Since the material transforms from a insulating dielectric to a conducting material during ablation, the attenuation factor will change as well. We assume κ depends on ρ as follows

$$\kappa(\rho) = \begin{cases} 0 & \rho \leq 0 \\ (2\kappa_1 - 4\kappa_2)\rho^2 + (4\kappa_2 - \kappa_1)\rho & 0 < \rho < 1 \\ \kappa_1 & \rho \geq 1 \end{cases} \tag{II.15}$$

where κ_1 is the room temperature, undamaged absorption coefficient of sapphire, κ_2 is the absorption coefficient at $\rho = 0.5$ due to electronic structure changes in the excited state. The motivation for the complicated attenuation factor is as follows. The maximum value of κ needs to be large enough such that the skin depth is on the order (or smaller) than the ablation depth. Otherwise E is approximately uniform throughout the model depth and the model will produce complete ablation or lack thereof through the entire model. We can therefore conclude that a maximum attenuation of $\kappa > 10^7 \mathrm{m}^{-1}$. While experimental data on sapphire is limited for this particular parameter, we can estimate $\kappa_1 < 10^{-3}\mathrm{cm}^{-1}$ for $\lambda = 355$ nm.[3,20]

The attenuation factor, κ is generally a non-trivial function of other material parameters. Different models have been created for approximating κ. One approximation based on optics in linear dielectrics crystals is given by

$$\kappa \propto \beta q^2 \tag{II.16}$$

where q is the effective charge and β is a damping parameter.[17] In this case, we have the effective charge q evolve as

$$q(\rho) = \begin{cases} 0 & \rho \leq 0 \\ (2q_1 - 4q_2)\rho^2 + (4q_2 - q_1)\rho & 0 < \rho < 1 \\ q_1 & \rho \geq 1 \end{cases} . \tag{II.17}$$

Since there is uncertainty in the validity of these approximations, we will use Bayesian statistics to judge its relevance in predicting laser ablation of sapphire.

II.D. Summary

Due to the amount of uncertainty in the coupling of the equations, two different constitutive models are considered.

- The first model uses the nonlinear Beer attenuation of the field, electronic structure evolution and a constant q with varying κ based on (II.15).
- The second model uses the nonlinear Beer relation, the electronic structure evolution equation, and a varying q with κ based on q and β as given by (II.16).

The models are referred to as the standard force model and the coupled force model, respectively, where the latter model includes coupling between parameters in (II.16). An overview of the different models is given in Table 1. Note that $\mathrm{H}(x)$ is the Heaviside function in several functions listed in the table.

Table 1. Summary of models tested. Parameters which are unmentioned are assumed to be deterministic. Parameters in the left column are treated as random parameters.

Name	Forced Model
Material evolution	$\beta\frac{\partial\rho}{\partial t} = a(\rho-1)(\rho-\frac{1}{2})(\rho) - \gamma$
Electromagnetics	$\frac{\partial\langle\lvert E\rvert\rangle}{\partial x} = -\kappa\langle\lvert E\rvert\rangle$
	$\gamma = \lvert qE\rvert$
$\theta = [q, \kappa_1, \kappa_2, a, \beta]$	$q = q\mathrm{H}(\rho)$
	$\kappa(\rho) = \begin{cases} 0 & \rho \le 0 \\ (2\kappa_1 - 4\kappa_2)\rho^2 + (4\kappa_2 - \kappa_1)\rho & 0 < \rho < 1 \\ \kappa_1 & \rho \ge 1 \end{cases}$
Name	Coupled Force Model
Material Evolution	$\beta\frac{\partial\rho}{\partial t} = a(\rho-1)(\rho-\frac{1}{2})(\rho) - \gamma$
Electromagnetics	$\frac{\partial\langle\lvert E\rvert\rangle}{\partial x} = -\kappa\langle\lvert E\rvert\rangle$
γ	$\gamma = \lvert qE\rvert$
$\theta = [q_1, q_2, a, \beta]$	$q(\rho) = \begin{cases} 0 & \rho \le 0 \\ (2q_1 - 4q_2)\rho^2 + (4q_2 - q_1)\rho & 0 < \rho < 1 \\ q_1 & \rho \ge 1 \end{cases}$
	$\kappa = \beta q^2$

III. Numerical Approximation and Simulation

In all examples we use a finite difference approximations to solve the governing equations. In the case where the original equations are reduced to an ODE, a forward Euler is used for the nonlinear equation while a backward Euler is used in the linear case.

III.A. Numerical Implementation

The numerical implementation of the nonlinear Beer relation in (II.8) is given by a backward Euler scheme

$$E^{i+1} = \frac{E^i}{1+\kappa\Delta x} \tag{III.1}$$

which has been verified against theory using the value $\kappa = 5\times10^8$ m^{-1} along with $\Delta x = \frac{100\text{ nm}}{4096}$ to provide sufficiently low errors.

The sharp interface model given by (II.3) is implemented using a forward Euler scheme

$$\rho^{i+1} = \rho^i + \frac{-a\Delta t}{\beta}(\rho^i-1)(\rho^i-\frac{1}{2})(\rho^i) + \frac{-|\gamma^{i+1}|\Delta t}{\beta} \tag{III.2}$$

where superscripts represent the time step. Figure 1 shows results converge to the equilibrium values of $\rho = 0$ and $\rho = 1$ when $E = 0$ and the initial value for the density was a linear function of x. The results illustrate converengence to a sharp interface at $x = 1$.

The initial conditions for ρ in the remaining analysis is

$$\rho = \begin{cases} 0 & x < 0 \\ 1 & x \ge 0 \end{cases} \tag{III.3}$$

which describe air for $x < 0$ and sapphire for $x \ge 0$. Note that Figure 1 does not represent these initial conditions, but instead illustrates that the initial condition in (III.3) is an equilibrium state.

The following approximation is used for γ

$$\gamma^i = |q\boldsymbol{E}^i| \tag{III.4}$$

where the superscript, i, denotes the time step.

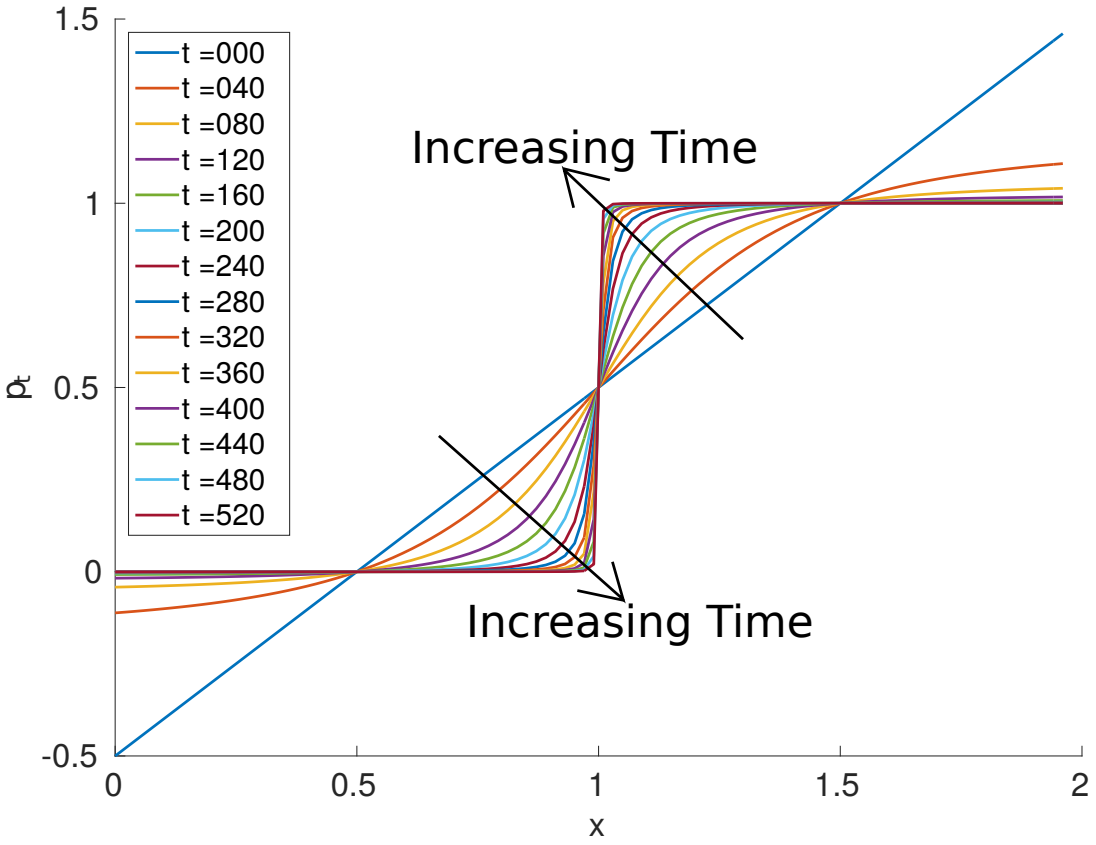

Figure 1. Numerical approximation for verification of our sharp interface model. This figure does not show the initial conditions of (III.3). Here, t represents the number of time steps.

Figure 2 shows convergence to a singular ablation depth value as both Δt and $\Delta x = \frac{l}{N}$ decrease. N is the number of points and l is the model length. Sufficient convergence is found for $\Delta t = 1$ fs and $\Delta x = \frac{1}{4096 x_0} \approx 24.4$ pm where x_0 is the model length $x_0 = 100$ nm. This temporal and spatial step size is used throughout the rest of the analysis.

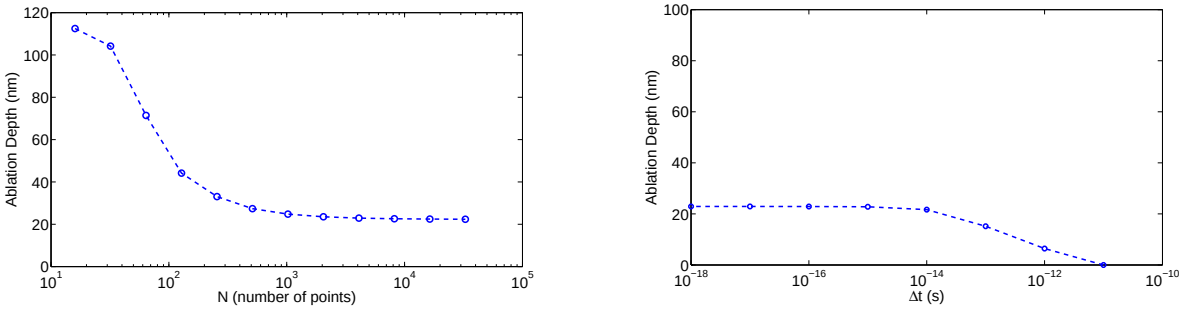

(a) Number of spatial points, N

(b) Time step size, Δt

Figure 2. Convergence of solutions for number of spatial points, N, and time step size, Δt. The time step is $\Delta t = 10^{-15}$ and $N = 4096$ unless otherwise stated.

III.B. Uncertainty Quantification

Since the physics involved in laser ablation is highly complex, uncertainty quantification is crucial to judge and validate the light-matter model predictions. Bayesian model calibration is built upon the assumption that calibration parameters exhibit uncertainty due to model discrepancies and experimental uncertainty. Therefore, uncertainty analysis provides a parameter distribution based on a sum-of-squares distribution error between the model and the data in conjunction with a prior density. The resulting likelihoods are then used to judge the uncertainty of the model parameters based on the difference between measurements and the model output. Details outlining this methodology are given by R. Smith in Chapter 8.[21]

The statistical model that will be used in subsequent sections is

$$s^{\text{data}}(i) = s(i;\theta) + \epsilon_i \tag{III.5}$$

for $i = 1, \ldots N$ data points, where s^{data} is the experimental ablation depth and ϵ_i is ith observational error. $s(i;\theta)$ is the model response and θ denotes the model parameters. The observation error can include error due to material difference, processing differences, measurement error and model errors.

Calibration uses Bayes' relation

$$P\left(\theta|s^{\text{data}}\right) = \frac{P(s|\theta)\pi_0(\theta)}{\int_{\mathbb{R}^n} P(s|\theta)\pi_0(\theta)\mathrm{d}\theta} \tag{III.6}$$

to determine the posterior density $P(\theta|s^{\text{data}})$ which is the probability of having parameters θ given s^{data} as the observed experimental data. π_0 represents the prior density, i.e. our *a priori* knowledge of the parameters. An uninformed prior (i.e. flat prior) is used for all analyses. That is the prior has equal probability across the entire support. $P(s|\theta)$ is the likelihood of the model results matching data given θ. The denominator is the normalization constant.

For independent and identically distributed (iid) normal errors, the likelihood is given by

$$P(s|\theta) = \mathrm{e}^{-\sum_{i=1}^{N}(s^{\text{data}}(i) - s(i;\theta)^2/2\sigma^2} \tag{III.7}$$

where σ^2 is the variance of the error which is unknown *a priori* and will be inferred from the calibration process along with θ.

There is a large range of model parameter values which map to either the full model depth, x_0 or 0 ablation. Therefore, a slight modification of the likelihood function is given as follows

$$P(s|\theta) = \mathrm{e}^{-f(\theta)} \tag{III.8}$$

where $f(\theta)$ is

$$f(\theta) = \begin{cases} \infty & \min(s(i;\theta)) \geq x_0 \\ \infty & \max(s(i;\theta)) \leq 0 \\ \sum_{i=1}^{N} \left(s^{\text{data}}(i) - s(i;\theta)^2\right)/2\sigma^2 & \text{otherwise} \end{cases} \tag{III.9}$$

This gives a zero probability in the areas where the parameters are not identifiable.

Unfortunately the computational cost of each model run, prohibits looking at very long chains. Therefore, several iterations of shorter chains typically of 25,000 iterations were used and the posterior density of the previous chain was used for the initial guess of the next chain. An assessment of the "burn-in" of chains to a converged posterior density will be included for each model. Uncertainty quantification is implemented in MATLAB using an algorithm distributed by Marko Laine.[22,23]

The results from both of the models will be presented individually. The results begin with a randomized, uninformed search over a single intensity. A few parameter points are taken from the resulting search based on a combination of minimizing error over all intensities and physical limits of the material parameters. Some points are taken based on physical intuition of parameter estimates, while others are chosen strictly because they have the smallest error over all intensities of an uninformed search. After the initial parameter analysis, model calibration is performed. The Markov Chain Monte Carlo (MCMC) is implemented numerically use the Delayed Rejection and Adaptive Metropolis (DRAM)[23] algorithm to quantify model uncertainty and validity in light of experimental results.

III.C. Standard Force Model

As a reminder, the equations for the standard force model are given in Table 1 and key parameters are given in Table 2. Global search results are presented first in the form of scatter plots. These global search results are used as a starting point for running MCMC DRAM model calibration. This provides a set of statistical measures used to assess the predictability and behavior of the model in light of data.

Initially global scatter plots are calculated to give an estimate of the model response as shown in Figure 3. Scatter plot results are performed on an order of magnitude uniform distribution using

$$\theta_i \sim 10^{U[(b_1,b_2)]} \tag{III.10}$$

where $\theta = \{a, \beta, \sigma_1, \sigma_2\}$, θ_i the ith element, 10^{b_1} and 10^{b_2} are the minima and maxima of the parameter space of θ_i and $U(b_1, b_2)$ is a uniform distribution on the interval (b_1, b_2). These plots can be thought of as realizations of conditional probability. The graphs also represent a coarse search of nearly the entire parameter space. The large number of values with an ablation depth 100 nm is due to the limit of model depth which is $d = 0.1$ μm.

We seek to fit the parameters based on knowledge of the valid parameter ranges plotted in Figure 3. However all three parameters β, a and q in (II.3) are not identifiable with (II.9) as described by the material kinetics equation

$$\frac{\partial \rho}{\partial t} = \frac{a}{\beta}(\rho - 1)(\rho - \frac{1}{2})(\rho) - \frac{|qE|}{\beta}. \tag{III.11}$$

A reasonable value of $\beta = 10^{-13}$ $\frac{\text{Ns}}{\text{m}^3}$ is selected based on the excitation time for electrons in sapphire. In addition, for values of κ_1 ranging from 10^{-10} m^{-1} to 10^5 m^{-1} the model is insensitive to changes in κ_1. Since we know physically that κ_1 is small, $\kappa_1 = 10^{-7}$ m^{-1} is arbitrarily chosen. MCMC simulations using DRAM are then used for parameter fitting and uncertainty analysis. Results are shown in Figure 4 and Table 3. In

Table 2. Key parameters for standard force model

Variable Name	Physical Representation
κ_1 m^{-1}	Attenuation of light in pristine sapphire
κ_2 m^{-1}	Maximum attenuation of light while sapphire undergoes ablation
q $\frac{\text{C}}{\text{m}^3}$	Effective electrical charge
β $\frac{\text{Ns}}{\text{m}^3}$	Damping parameter
a $\frac{\text{N}}{\text{m}^3}$	Landau parameter – effectively governs bond strength

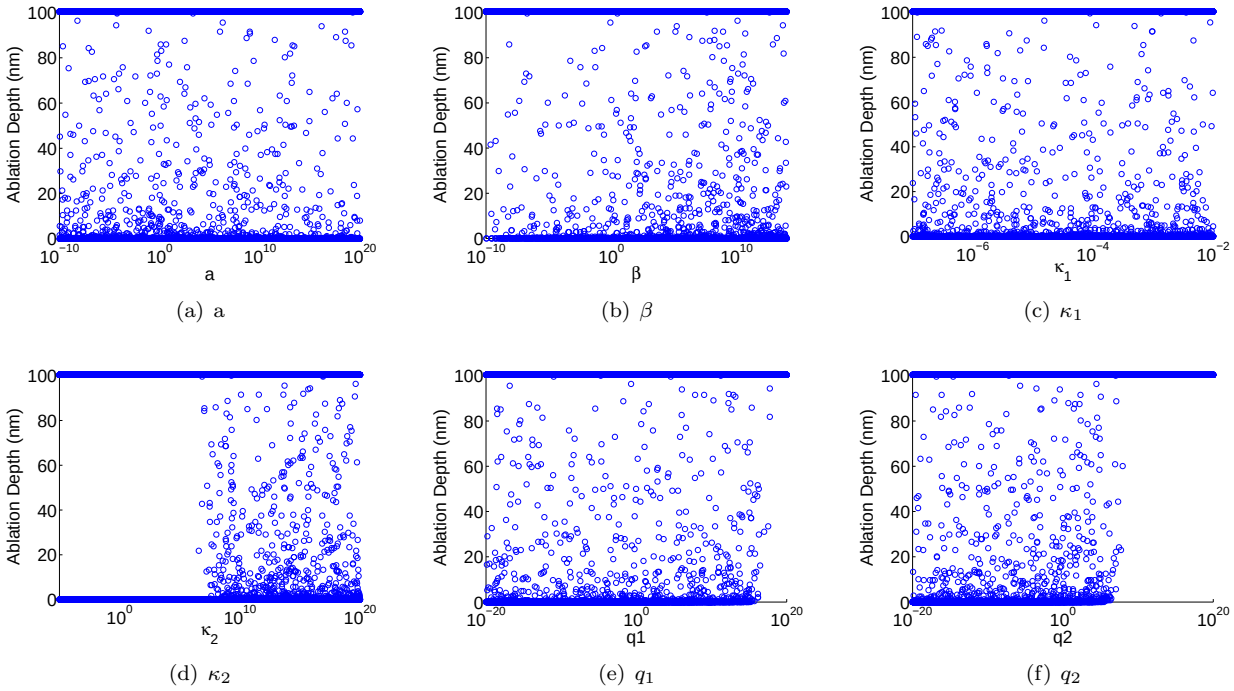

(a) a (b) β (c) κ_1

(d) κ_2 (e) q_1 (f) q_2

Figure 3. Global scatter plots for the six material parameters with 100,000 points for the standard force model.

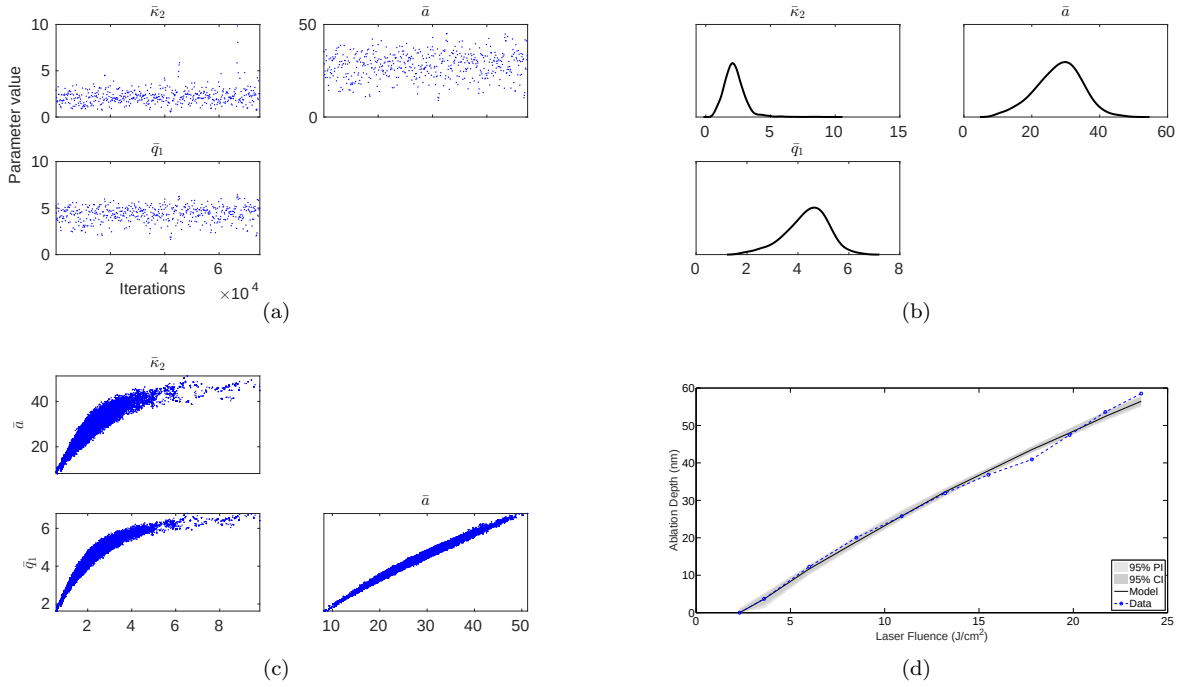

Figure 4. These figures show the convergence of our parameters using a DRAM algorithm. In this case the mobility is fixed at $\beta = 10^{-13}\ \frac{\text{Ns}}{\text{m}^3}$. (a) The chains show the last 75,000 iterations. (b) Posterior densities of the model parameters (c) Pair correlations (d) Model prediction including 95 % prediction intervals (PI) and 95 % credible intervals (CI). iterations. Mean parameter values are given in Table 3.

Figure 4, some of the parameter values have been scaled. Specifically $\bar{\kappa} \times 10^9 = \kappa$ and $\bar{q_1} \times 10^{-10} = q_1$ where the barred values are shown in the figures.

The time constants for ablation can be estimated using $\tau = \frac{\beta}{a}$. In the standard force model model $\tau = 3.5 \times 10^{-3}$ ps which is smaller than estimations of the electron relaxation time $\tau_e \approx 100$ ps.[14]

Table 3. Summary of mean and standard deviations from the Monte Carlo Analysis shown in Figure 4. In this case the mobility is fixed at $\beta = 10^{-13}\ \frac{\text{Ns}}{\text{m}^3}$.

Parameter	Mean	Standard Deviation
κ_2	2.2×10^9	8.6×10^8
a	28	6.8
q_1	4.4×10^{-10}	$8.4 \times 10{-}11$

Local sensitivity results are presented in Figure 5 to complement the posterior densities in Figure 4. In these figures, the parameters are set to the values presented in Table 3. In each figure only one of the parameters is varied from results in Table 3 while holding the other parameters at their mean values.

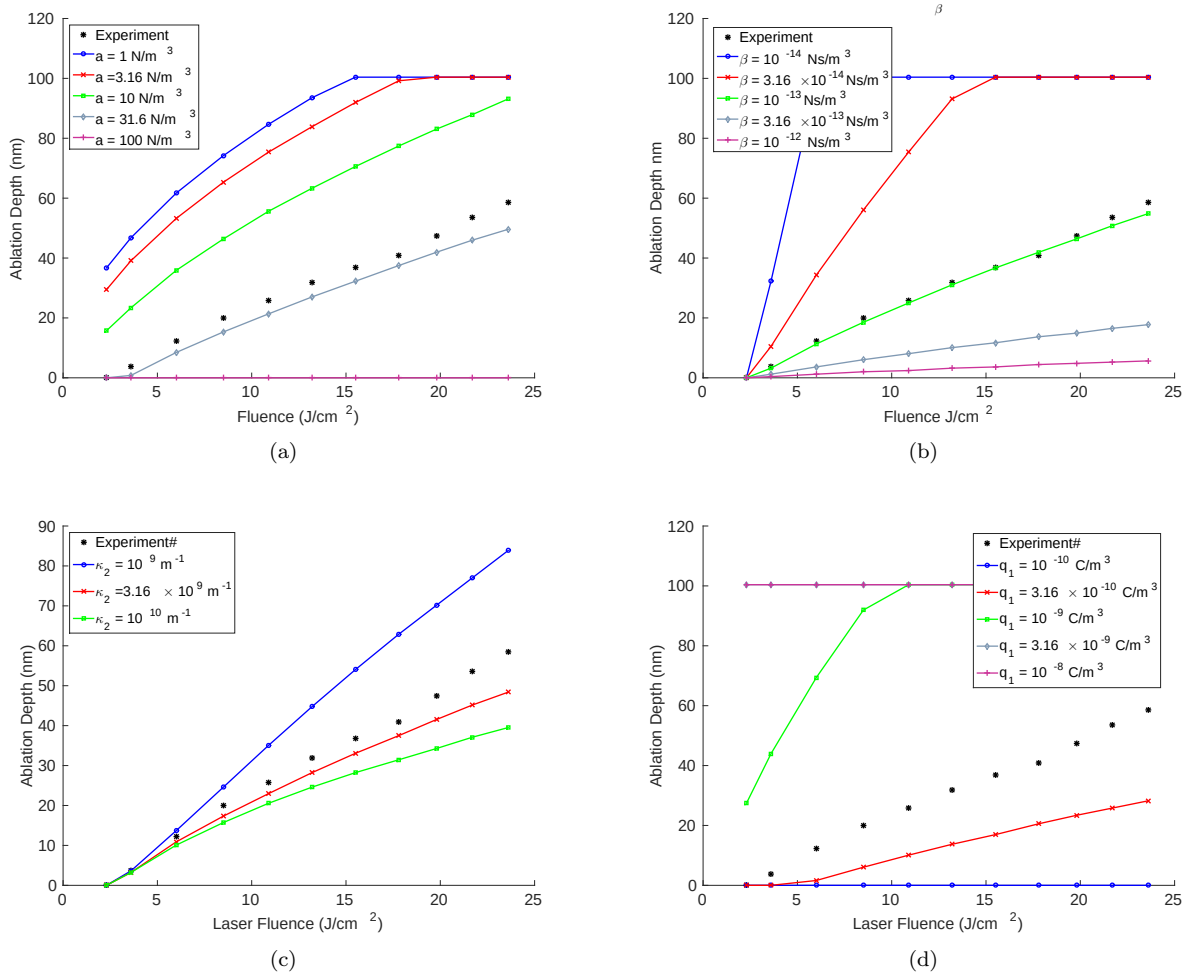

Figure 5. Local sensitivities of key material parameters about the the mean values given in Table 3 for the standard force model. The parameter varied in these simulations is given in the legend with all other values held fixed at their mean values.

III.D. Coupled Force Model

As a reminder, the coupled force model is given by the governing equations in Table 1 and key parameters given in Table 4. Note that by implementing the constitutive equation, $\kappa = \beta q^2$, all the parameters become identifiable.

It is important to note that the parameters from (II.3) have been scaled by a factor of $\beta_0 = 10^{-13}\ \frac{\text{Ns}}{\text{m}^3}$ as follows

$$\bar{\beta}\frac{\partial \rho}{\partial t} = -\bar{a}(\rho - 1)(\rho - \frac{1}{2})(\rho) + |\bar{q}E| \tag{III.12}$$

Table 4. Key parameters for coupled force model

Variable Name	Physical Representation
q_1	Effective electrical charge in pristine sapphire
q_2	Effective electrical charge while sapphire undergoes ablation
β	Damping parameter
a	Landau parameter – effectively governs bond strength

where $\bar{a} = \frac{a}{\beta_0}$, $\bar{\beta} = \frac{\beta}{\beta_0}$ and $\bar{q} = \frac{q}{\beta_0}$.

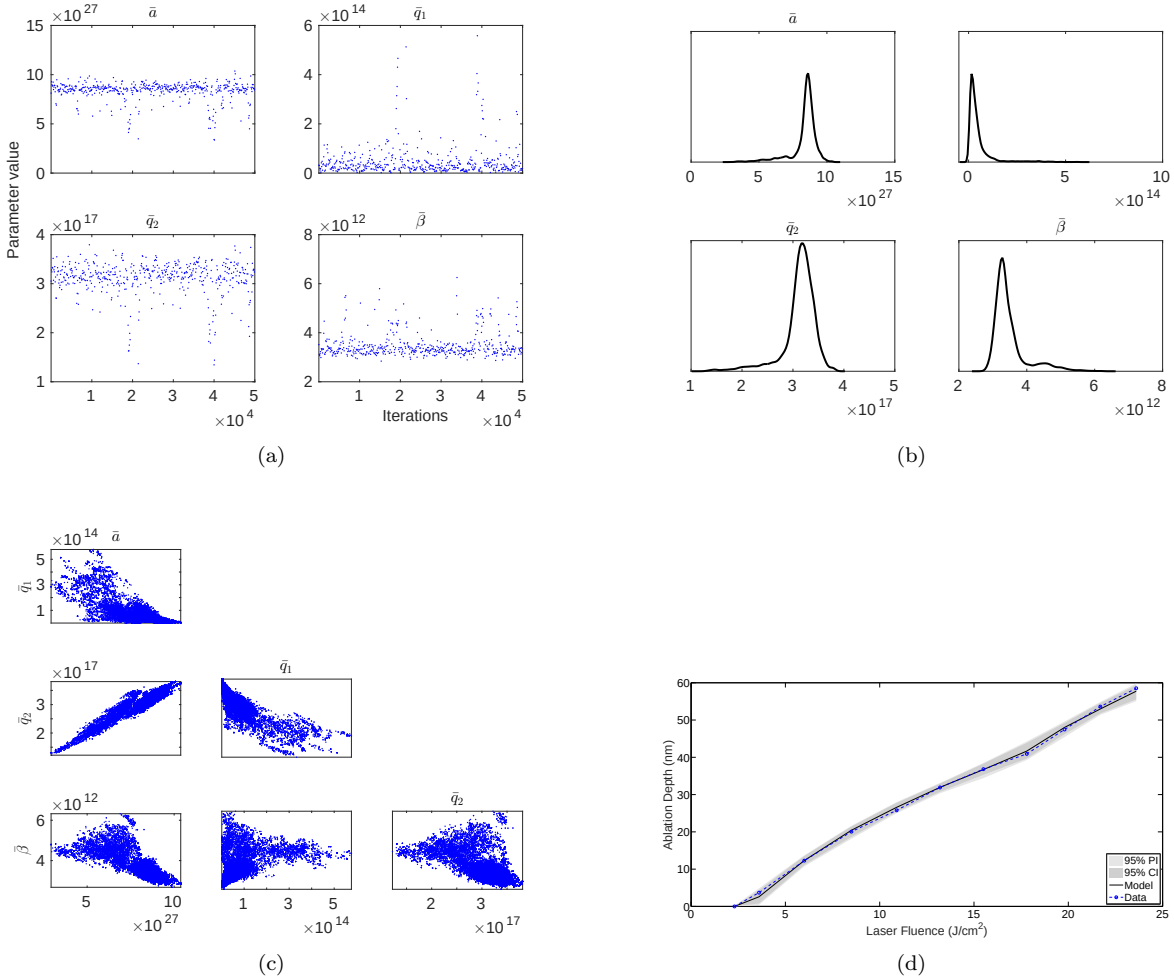

Figure 6. These figures show the convergence of our parameters through a DRAM algorithm. The chains show the last 50,000 iterations. 200,000 iterations were performed prior to this analysis. Mean parameter values are given in Table 5. (a) The chains show the last 75,000 iterations. (b) Posterior densities of the model parameters (c) Pair correlations (d) Model prediction including 95 % prediction intervals (PI) and 95 % credible intervals (CI).

Figure 6 shows the results from the MCMC DRAM search. Two important points can be made. First, the attenuation of light in pristine sapphire for these parameters is $\kappa \approx 8\ \mathrm{m}^{-1} = .08\ \mathrm{cm}^{-1}$ which is a reasonable parameter.[20] When you account for scaling the parameters, the parameter values are not significantly different from the ones found in the standard force model. The minimal amount of correlation in Figure 6(c) suggests the constitutive relation $\kappa = \beta q^2$ provides more fundamental estimates of picosecond laser ablation in sapphire. The comparative unscaled values can be found in Table 6. The time constant $\tau = 4.2 \times 10^{-4}$ ps is again faster than expected, but similar to the model presented in the previous section.

Table 5. This table shows the mean and standard deviation from the Monte Carlo Analysis in the results shown in Figure 6.

Parameter	Mean	Standard Deviation
a	8.3×10^{14}	9.8×10^{13}
q_1	4.8	6.5
q_2	3.1×10^{4}	3.4×10^{3}
β	0.35	0.0049

Table 6. Table comparing the different parameter values between the two constitutive relations. Note that in the coupled force model, κ_1 and κ_2 are calculated use $\kappa = \beta q^2$. κ_1 was unidentifiable in the first model due to it's insensitivity. This explains the discrepancy between $kappa_1$ in the two models. β was unidentifiable in the first model, so the more relevant comparisons of $\tau = \frac{\beta}{a}$ and $\frac{\beta}{q_1}$ are included as well.

Parameter	Standard Force Model	Coupled Force Model
κ_1 (m^{-1})	10^{-9}	8.1
κ_2 (m^{-1})	2.2×10^{9}	3.4×10^{8}
a $(\frac{\mathrm{N}}{\mathrm{m}^3})$	28	8.3×10^{14}
q_1 $(\frac{\mathrm{C}}{\mathrm{m}^3})$	5×10^{-10}	6.5
q_2 $(\frac{\mathrm{C}}{\mathrm{m}^3})$	N/A	3.1×10^{3}
β $(\frac{\mathrm{Ns}}{\mathrm{m}^3})$	10^{-13}	0.35
$\tau = \frac{\beta}{a}$ (ps)	2.4×10^{-3}	4.2×10^{-4}
$\frac{\beta}{q_1}$	2×10^{-4}	7.3×10^{-3}

IV. Conclusions

In this paper, a sharp interface model for laser ablation is presented. The sharp interface model is defined in the limit of the phase-field model as the diffusion term goes to zero. Two different formulations based on the electronic force are provided. The second formulation provides an improved constitutive law to reduce the number of unidentifiable parameters. Both formulations provide a robust model amenable to direct correlations with experimental operating conditions which can be used to directly correlate the modeling with experiments of the ablation process. Both formulations matched data well with a sum of square error < 5 nm per fluency data point. In general, parameter estimation matched the parameters within their expected values. The only exception to this is the time constant $\tau \approx 3$ fs which is significantly less than the expected relaxation time of electrons $\approx$ 100ps. The relaxation time only functions as an upper bound for the correct time constant and it is unclear how τ should relate to this upper bound. Furthermore we noted that $\kappa \propto \beta q^2$. The actual linear dielectric formula is given by

$$\kappa = \frac{N q_e^2 \omega^2}{2 m_e \epsilon_0 c} \sum_j \frac{f_j \beta_j}{(\omega_j^2 - \omega_2)^2 + \beta_j^2 \omega^2} \tag{IV.1}$$

where N is the number of electrons per unit volume, q_e is the electron charge, m_e is the electron mass, ω is the laser frequency, ω_j is the natural frequency of the jth state, c is the speed of light, ϵ_0 is the permittivity of free space, f_j is the degeneracy of jth state and β_j is the damping of each state. In the approximation of $\omega >> \omega_j$, $\omega >> \beta_j$ and that all electrons can be treated as in identical states, this reduces to

$$\kappa = \frac{N^2 q_e^2 \beta}{2 m_e \epsilon_0 c \omega^2} = \frac{q^2 \beta}{2 m_e \epsilon_0 c \omega^2}. \tag{IV.2}$$

This term gives $\kappa \approx 580 \beta q^2 = \bar{\beta} q^2$. Thus is we take $\bar{\beta}$ as the value given by the calculations, our time constant changes to 240 fs. While this increase the time constant, *tau* is still less than thr upper bound of the electron relaxation time: 100 ps. While this modification keeps κ constant it affects the material kinetics. These parameters no longer match data which leaves the appropriate parameter selection an open question.

We conclude that the model formulations are similar as both models successfully predict laser ablation on the picosecond pulsed time scale. As such, the second model is recommended as a better choice for future analysis since it is a simpler formulation in which all model parameters can be estimated from laser ablation data.

IV.A. Acknowledgements

The authors wish to gratefully thank the United States Department of Energy for providing funds to support this research under grant DOE-FE0012370.

References

[1]Chen, T.-C. and Darling, R. B., "Parametric studies on pulsed near ultraviolet frequency tripled Nd:YAG laser micromachining of sapphire and silicon," *Journal of Materials Processing Technology*, Vol. 169, No. 2, 2005, pp. 214 – 218.

[2]Wang, X., Lim, G., Zheng, H., Ng, F., Liu, W., and Chua, S., "Femtosecond pulse laser ablation of sapphire in ambient air," *Applied Surface Science*, Vol. 228, No. 14, 2004, pp. 221 – 226.

[3]Blood, D., *Simulation, Part Path Correction, and Automated Process Parameter Selection for Ultrashort Pulsed Laser Micromachining of Sapphire*, Ph.D. thesis, University of Florida, 2014.

[4]Rothenberg, J. E. and Koren, G., "Laser produced plasma in crystalline α-Al_2O_3 and aluminum metal," *Applied Physics Letters*, Vol. 44, April 1984, pp. 664–666.

[5]Han, J., Li, C., Zhang, M., Zuo, H., and Meng, S., "An investigation of long pulsed laser induced damage in sapphire," *Optics & Laser Technology*, Vol. 41, No. 3, 2009, pp. 339 – 344.

[6]Jiang, L. and Tsai, H.-L., "A plasma model combined with an improved two-temperature equation for ultrafast laser ablation of dielectrics," *Journal of Applied Physics*, Vol. 104, No. 9, Nov. 2008, pp. 093101.

[7]Bäuerle, D., *Laser Processing and Chemistry*, Vol. 4, Springer, 2011.

[8]Ashkenasi, D., Rosenfeld, A., Varel, H., Whmer, M., and Campbell, E., "Laser processing of sapphire with picosecond and sub-picosecond pulses," *Applied Surface Science*, Vol. 120, No. 12, 1997, pp. 65 – 80.

[9]Dreyfus, R. W., Kelly, R., and Walkup, R. E., "Laser induced fluorescence studies of excimer laser ablation of Al_2O_3," *Applied Physics Letters*, Vol. 49, 1986, pp. 1478 – 1480.

[10]Dreyfus, R. W., McDonald, F. A., and von Gutfeld, R. J., "Laser energy deposition at sapphire surfaces studied by pulsed photothermal deformation," *Applied Physics Letters*, Vol. 50, No. 21, 1987, pp. 1491–1493.

[11]Ashkenasi, D., Stoian, R., and Rosenfeld, A., "Single and multiple ultrashort laser pulse ablation threshold of Al_2O_3 (corundum) at different etch phases," *Applied Surface Science*, Vol. 154155, No. 0, 2000, pp. 40 – 46.

[12]Ashkenasi, D., Lorenz, M., Stoian, R., and Rosenfeld, A., "Surface damage threshold and structuring of dielectrics using femtosecond laser pulses: the role of incubation," *Applied Surface Science*, Vol. 150, No. 14, 1999, pp. 101 – 106.

[13]Manenkov, A. A., "Fundamental mechanisms of laser-induced damage in optical materials: todays state of understanding and problems," *Optical Engineering*, Vol. 53, No. 1, 2014, pp. 010901.

[14]Li, X., Jia, T., Feng, D., and Xu, Z., "Ablation induced by femtosecond laser in sapphire," *Applied Surface Science*, Vol. 225, No. 14, 2004, pp. 339 – 346.

[15]Moelans, N., Blanpain, B., and Wollants, P., "An introduction to phase-field modeling of microstructure evolution," *Calphad*, Vol. 32, No. 2, 2008, pp. 268 – 294.

[16]Nelson, D. F., *Electric, Optic and Acoustic Interactions in Dielectrics*, John Wiley and Sons Inc, 1979.

[17]Griffiths, D. J., *Introduction to Electrodynamics*, Pearson Education Inc., 1999.

[18]Sun, M., Eppelt, U., Russ, S., Hartmann, C., Siebert, C., Zhu, J., and Schulz, W., "Laser ablation mechanism of transparent dielectrics with picosecond laser pulses," *Proc. SPIE*, Vol. 8530, 2012, pp. 853007–853007–10.

[19]D. Corbett and M. Warner, "Bleaching and stimulated recovery of dyes and of photocantilevers," *Phys. Rev. E*, Vol. 77, 2008, pp. 051710.

[20]Dobrovinskaya, E. R., Lytvynov, L. A., and Pishchik, V., *Sapphire Material, Manufacturing Applications*, Springer, 2009.

[21]Smith, R. C., *Uncertainty Quantification Theory, Implementation, and Applications*, SIAM, Philadelphia, Pennsylvania, 2014.

[22]H. Haario, M. Laine, A. M. and Saksman, E., *DRAM - Delayed Rejection Adaptive Metropolis*, 2011, (accessed January 22, 2015).

[23]Haario, H., Laine, M., Mira, A., and Saksman, E., "DRAM: Efficient adaptive MCMC," *Statistics and Computing*, Vol. 16, No. 4, 2006, pp. 339–354.